Nano Research

Open Access

Research Article

Nitrogen-free charge-asymmetric indium cluster catalyst for efficient CO_2 electroreduction to formate

Xi Li[1], Yuanting Lei[2], Yan Gao[3] ✉, Huishan Shang[2] ✉, Fan Yang[1] ✉, and Yongfeng Li[1] ✉

[1] *College of New Energy and Materials, China University of Petroleum, Beijing 102249, China*
[2] *School of Chemical Engineering, Zhengzhou University, Zhengzhou 450001, China*
[3] *AnHui Provincial Engineering Research Center of Silicon-Based Materials, Bengbu University, Bengbu 233030, China*

Cite this article: *Nano Research*, **2025**, *18*, 94907370. https://doi.org/10.26599/NR.2025.94907370

ABSTRACT: Electrochemical CO_2 reduction reaction (CO_2RR) into high-value chemicals and fuels is recognized as a promising strategy for mitigating energy and environmental challenges. However, this process frequently faces limitations due to inadequate selectivity towards specific products and insufficient electrochemical stability. Main group indium (In) catalysts have emerged as promising materials for CO_2RR to highly valued formate. In this study, we constructed an indium cluster material with charge-asymmetric atomic structure anchored on nitrogen-free carbon nanoframeworks (designated as In Clu/C), which exhibits exceptional efficiency as a CO_2RR catalyst for formate production. Notably, the In Clu/C achieves a remarkable formate Faradaic efficiency of 98.7% at −0.70 V. Furthermore, *in-situ* X-ray absorption spectroscopy (XAS) measurements reveal that the superior catalytic performance can be attributed to partially positively charged $In^{\delta+}$ ($0 < \delta < 3$) active sites. This discovery may provide new insights into the precise synthesis of metal cluster catalysts for environmental and energy applications.

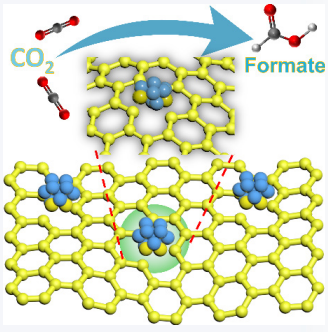

KEYWORDS: indium cluster catalyst, nitrogen-free carbon framework, charge asymmetry structure, CO_2 reduction reaction, formate

1 Introduction

The excessive emission of CO_2 from industrial activities has led to an increasingly severe greenhouse effect in the atmosphere. The conversion of CO_2 into higher-value products using green and environmentally friendly electrical energy is attracting growing attention, representing a viable strategy to address environmental and energy challenges [1–6]. To date, the electrochemical CO_2 reduction reaction (CO_2RR) continues to face significant challenges due to the chemical inertness of CO_2 molecules and the complexity of electron transfer processes [7–12]. Consequently, the discovery of CO_2RR electrocatalysts with high efficiency to promote reaction kinetics and achieve superior selectivity toward desired products is both significant and urgent. C_1 products, including carbon monoxide (CO), methanol (CH_3OH), methane (CH_4), and formate (HCOOH), have garnered significant attention. Notably, formate is a valued industrial product with applications in efficient hydrogen storage. A broad spectrum of metal-based catalysts, encompassing both precious metals (such as Ru, Pd, Ag, and Au) and earth-abundant elements (such as Cu, Ni, and Co), has been extensively investigated using experimental and computational methods to enhance their CO_2RR performance and selectivity toward various target products [13–18]. However, these catalysts generally exhibit unsatisfactory selectivity toward formate. Recently, main group metals, including indium (In), tin (Sn), antimony (Sb), and bismuth (Bi), have garnered significant attention due to their potential to achieve high catalytic activity and selectivity in formate production [19–22]. Sn and Bi, renowned for their affordability and cost-effectiveness, have been extensively investigated. In contrast, In, which is positioned adjacent to Sn and Sb in the periodic table, remains relatively underexplored for CO_2RR despite its potential. Although bulk In exhibits limited formate selectivity, the implementation of nanostructure engineering strategies has proven effective in enhancing selectivity [23–26]. Nevertheless, the development of suitably configured In-based catalysts for efficient CO_2RR to produce formate requires further exploration.

Both theoretical and experimental studies show that metal cluster-nitrogen (M Clu-N_x) modified carbon-based materials are effective CO_2RR electrocatalysts with excellent performance. Nitrogen-doped carbon (NC) substrates provide anchor sites for metal

Received: January 27, 2025; **Revised:** March 5, 2025
Accepted: March 14, 2025

✉Address correspondence to Huishan Shang, shanghs@zzu.edu.cn; Fan Yang, yangfan@cup.edu.cn; Yongfeng Li, yfli@cup.edu.cn; Yan Gao, gaoyan@bbc.edu.cn

clusters and alter electronic structures by regulating the atomic interactions between the active sites and the coordination species. This enables the precise tuning of CO_2 adsorption energy, thereby enhancing CO_2RR performance [27–33]. Nevertheless, the utilization of nitrogen-containing compounds for etching carbon substrate introduces additional complexity into the synthesis procedure while simultaneously enabling the formation of monoatomic metal active centers. This occurrence is attributed to the high electronegativity of nitrogen species, which stabilizes isolated metal atoms through robust electronic interactions, thereby inhibiting their aggregation throughout the synthesis. Specifically, nitrogen-doped carbon-based materials are synthesized utilizing various nitrogen sources, including nitrogen-containing organic compounds, inorganic nitrogen sources, and biomass-derived nitrogen sources (for instance, urea, dicyandiamide, and chitosan). These materials undergo pyrolysis, leading to the generation of nitrogen-containing gases that facilitate the etching of the carbon matrix, thereby adding complexity to the catalyst preparation process. The key aspects of N-doping into carbon involve controlling the typical N-constituent types, which include pyridine-N, pyrole-N, graphitic-N, oxidized-N, and the recently discovered sp-hybridized N [34]. Ozkan and colleagues investigated the oxygen reduction reaction (ORR) performance of nitrogen-doped carbon through the incorporation of phosphoric acid. Their results demonstrated a linear decrease in specific kinetic current density as the phosphate anion concentration increased [35]. This phenomenon is attributed to the loss of catalytic activity caused by the protonation of pyrrole nitrogen, which is more pronounced in acidic solutions. However, different nitrogen configurations exhibit varying catalytic behaviors, and the intrinsic mechanism remains controversial. While it is feasible to control the relative proportions of nitrogen species, achieving this under synthetic conditions that involve metal clusters presents significant challenges. Consequently, considering the constraints associated with traditional nitrogen etching techniques, the direct application of carbon substrates for the stabilization of metal clusters emerges as a more advantageous alternative. Structurally symmetric active center configurations exhibit unsatisfactory catalytic activity. Introducing heteroatoms or modulating the spatial arrangement of these structures can disrupt this symmetry, thereby significantly improving catalytic performance [36–38]. Asymmetric coordination can regulate the electron distribution and spatial configuration of active centers, enhance the adsorption and desorption of intermediates, and reduce the free energy of the reaction [39–42]. In this study, we employed a straightforward approach to develop an In cluster catalyst with charge-asymmetric active sites supported on N-free carbon nanostructures (In Clu/C) for efficient CO_2RR to formate. The In Clu/C catalyst demonstrated a remarkable formate Faradaic efficiency of 98.7% at −0.70 V vs. reversible hydrogen electrode (RHE). Additionally, *in-situ* X-ray absorption spectroscopy revealed that the unique $In^{\delta+}$ active sites played a critical role in enhancing the CO_2RR performance for formate production.

2 Experimental

2.1 Synthesis of In-MOF

In summary, 30.0 mg of 1,4-benzenedicarboxylic acid and 78.0 mg of $In(NO_3)_3{\cdot}xH_2O$ were dissolved in 9.0 mL of N,N-dimethylformamide (DMF). The resultant solution was subjected to heating in an oil bath at 100 °C for a duration of 10 min. Following the heating period, the mixture was allowed to cool, and the resulting nanoparticles were subsequently collected via centrifugation. These nanoparticles were then washed multiple times with DMF and methanol.

2.2 Synthesis of In Clu/C

The obtained In-MOF precursor was placed in a porcelain boat and heated at 700 °C in a tube furnace (with a temperature increase rate of 2 °C/min) for 1 h under a nitrogen flow of 8 mL/min to produce In Clu/C. The indium content was determined to be 1.35 wt.% based on inductively coupled plasma optical emission spectrometry (ICP-OES) analysis.

2.3 Physicochemical characterization

The crystal structures of the samples were examined using powder X-ray diffraction (PXRD) patterns, recorded with a Bruker D8 Advance diffractometer at a scan rate of 5 °/min. Transmission electron microscopy (TEM) images were captured using a Tecnai G2 F20 S-Twin instrument operating at 200 kV. For TEM analysis, the samples were deposited onto carbon-coated copper grids that were immersed in ethanol solutions and subsequently dried at room temperature.

2.4 Electrochemical test

To prepare a catalyst ink with a strength of 2 mg/mL and ensure uniform distribution, 10 μL of a 5 wt.% Nafion solution and 2 mg of the catalyst were sonicated in a mixture of deionized water and ethanol (1:4 volume ratio) for at least 30 min. Electrochemical measurements were performed using a CHI 760E electrochemical workstation in a gas-tight H-type cell, containing 45 mL of 0.5 M $KHCO_3$ as the electrolyte. A Nafion 117 membrane separated the cathodic and anodic compartments. The counter electrode was a platinum plate, and an Ag/AgCl electrode (saturated with KCl) was used as the reference electrode. The electrode potential was calculated using the formula: $E_{RHE} = E_{Ag/AgCl} + 0.197\ V + 0.0591 \times pH$. A 10 μL volume of the catalyst ink was applied to a glassy carbon electrode with a surface area of 0.196 cm^2, yielding a catalyst loading of 0.102 mg/cm^2. Before measurements, CO_2 was introduced into the electrolyte for 20 min to saturate it with CO_2. Cyclic voltammetry (CV) was conducted in the CO_2-saturated 0.5 M $KHCO_3$ at a scan rate of 50 mV/s, while linear sweep voltammetry (LSV) was executed at a scan rate of 10 mV/s. For the stability tests, a larger H-cell containing 125 mL of anolyte and catholyte was utilized. The catalyst loading was set at 2.0 mg/cm^2 to prevent detachment, and the electrolyte was replaced after every 5 h of electrolysis. The RHE was used as the reference for all potentials.

3 Results and discussion

A method combined wet chemistry and pyrolysis was utilized to prepare the In Clu/C (Fig. 1(a)). Typically, In-MOF was prepared firstly (Figs. S1 and S2 in the Electronic Supplementary Material (ESM)), 30.0 mg (0.18 mmol) of 1,4-benzenedicarboxylic acid and 78.0 mg (0.26 mmol) of $In(NO_3)_3{\cdot}xH_2O$ were homogeneously dispersed in 9.0 mL of DMF under ambient conditions. The mixture was subsequently subjected to thermal treatment in an oil bath maintained at 100 °C for 10 min. Upon cooling to room temperature, the crystalline product was isolated via centrifugation (8000 rpm, 5 min) and sequentially purified through multiple

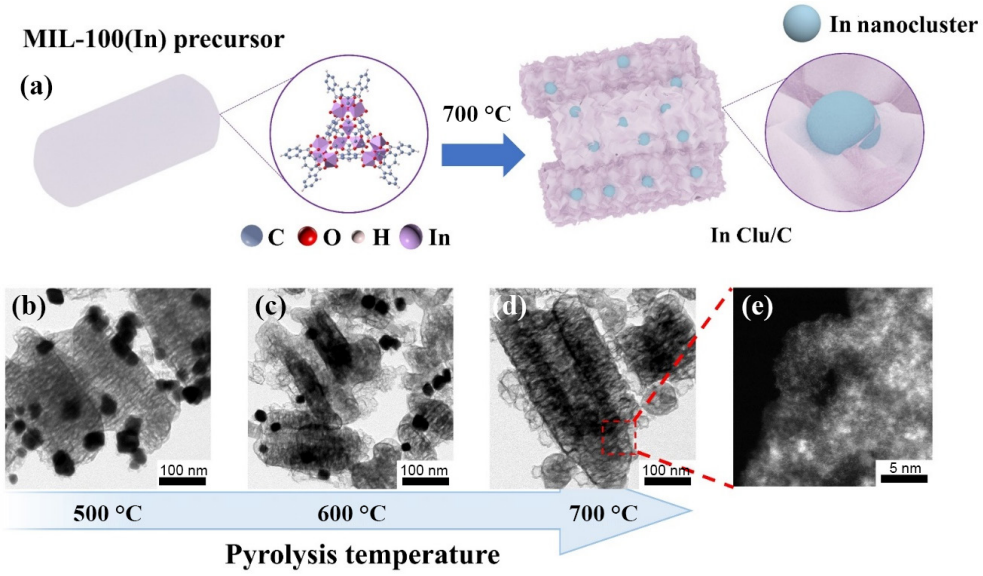

Figure 1 (a) Scheme of the synthesis from In-MOF to In Clu/C. (b)–(d) Representative TEM images of In-MOF pyrolyzed at different temperatures. (e) HAADF-STEM image of In Clu/C.

washing cycles with DMF and methanol to remove residual reactants and solvents. Then the In Clu/C was obtained after pyrolyzing the In-MOF at 700 °C under N_2 atmosphere, which ensured the formation of metal clusters and the removal of nitrate. Figures 1(b)–1(d) displayed the TEM images of In-MOF pyrolyzed at different temperatures (500, 600, and 700 °C). In the TEM image of the sample heated at 700 °C (Fig. 1(d)), no clear indium particles were observed. Scanning transmission electron microscopy (STEM) coupled with energy-dispersive X-ray spectroscopy (EDS) elemental mapping revealed a homogeneous distribution of indium across the structure (Fig. S3 in the ESM). The high-magnification high-angle annular dark-field STEM (HAADF-STEM) image (Fig. 1(e)) further confirmed the well-dispersed indium clusters, as evidenced by the clearly visible bright spots, which are anchored on the N-free carbon framework. The cluster size distribution of In Clu/C is mainly concentrated around 0.8 nm (Fig. S4 in the ESM).

In Fig. 2(a), the X-ray diffraction (XRD) pattern of In Clu/C exhibits a broad diffraction peak (002) and a small shoulder peak (010), attributed to graphitic carbon. No other impurity peaks were detected, further indicating the absence of large indium nanoparticles. Then the composition and chemical state of In Clu/C were monitored by X-ray photoelectron spectroscopy (XPS) tests. In Fig. 2(b), the XPS C 1s spectrum with high-resolution was deconvoluted into C–C/C=C (284.8 eV), and C–In (285.4 eV), and C=O (288.3 eV). The results in Fig. S5 in the ESM indicate that nitrogen atoms are not doped onto the carbon substrate, and carbon atoms are primarily bonded to indium within the metal clusters. This is mainly attributed to the removal of the nitrogen-containing precursor through thorough washing of the In-MOF. Moreover, soft X-ray absorption spectroscopy (sXAS) analysis was also carried out to further identify the electronic feature of C species in In Clu/C [43, 44]. The C K-edge spectrum of In Clu/C (Fig. 2(c)) exhibited three distinct peaks at 285.0, 288.2, and 292.4 eV, which are attributed to the π*C=C, π*C–In, and σ*C–C antibonding orbital orbitals. For comparison, indium single atoms (In SAC) and In NC samples were also synthesized and analyzed. As shown in Figs. S6 and S7 in the ESM, XRD pattern and HAADF-STEM imaging confirmed the dispersion of indium single atoms on the carbon support in the In SACs/C sample. Moreover, the results presented in Figs. S8 and S9 in the ESM demonstrate the co-existence of indium single atoms and clusters in the In NC sample.

To explore the local coordination structure of In Clu/C, hard X-ray absorption fine structure (XAFS) analysis was conducted [45–48]. Figure 2(d) displayed the X-ray absorption near edge structure (XANES) curve of In Clu/C at In K-edge. The absorption edge of In Clu/C located between In foil and In_2O_3, suggesting the distinct electronic state of $In^{\delta+}$ ($0 < \delta < 3$), resulting from the interactions between the indium clusters and the carbon substrate. As illustrated in Fig. 2(e), the Fourier-transformed (FT) EXAFS spectrum of In Clu/C shown a strong peak around 1.5 Å, which is attributed to In–O/C. In contrast, a clear In–In peak was observed around 3.0 Å, typical of indium foil, indicating that indium clusters were well-dispersed on the carbon matrix. To further confirm the atomic dispersion of indium clusters in In Clu/C, we performed wavelet transform (WT)-EXAFS analysis, as shown in Fig. 2(f). A strong WT signal at 4.9 and 12.4 $Å^{-1}$ was observed, corresponding to the In–C and In–In contributions, respectively, when compared to the WT contour plots of In_2O_3 and indium foil. The coordination environment of In Clu/C was quantitatively determined via least-squares EXAFS fitting (Figs. 2(g) and 2(h) and Table S1 in the ESM). For comparison, the EXAFS data of indium foil were also analyzed (as shown in Fig. S11 in the ESM) to calculate the amplitude reduction factor ($S0^2$), which was determined to be 0.82 [49]. The fitting results indicate that the average In–O/C bond distance is 1.95 Å, while the average In–In bond distance is 2.65 Å.

To assess the catalytic performance, CO_2RR experiments were conducted in a gas-tight H-type cell with CO_2-saturated 0.5 M $KHCO_3$ solution. LSV measurements were performed for both In Clu/C and In SACs/C catalysts (Fig. 3(a)). The onset potential and current density serve as key metrics for assessing electrocatalytic performance. Compared to In SACs/C and In NC (Fig. S12 in the ESM), In Clu/C exhibited a lower onset potential and a higher current density, indicating enhanced catalytic efficiency. To further investigate the selectivity of In Clu/C, Faradaic efficiency tests were performed. Gaseous products were analyzed in real-time using gas

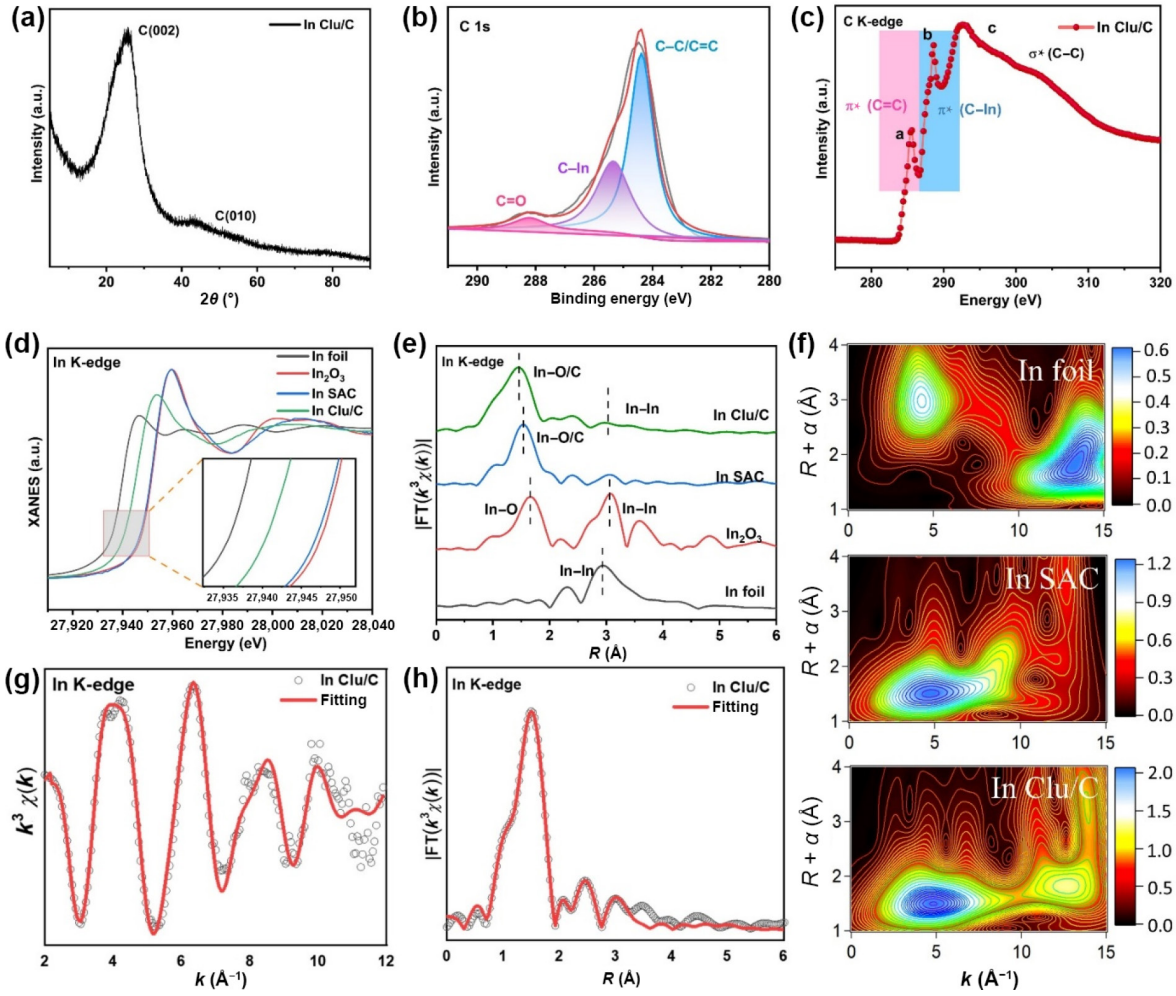

Figure 2 (a) XRD pattern of In Clu/C. (b) C 1s XPS spectra of In Clu/C. (c) C K-edge soft XAS spectrum of In Clu/C. (d) The In K-edge XANES spectra of In Clu/C and the references. (e) The FT-EXAFS spectra of In Clu/C and the references at In K-edge. (f) WT-EXAFS plots of In foil, In SACs/C and In Clu/C, respectively. (g) The *k* space EXAFS fitting curves of In Clu/C at In K-edge. (h) The FT-EXAFS fitting curves of In Clu/C at In K-edge.

chromatography (GC), while proton nuclear magnetic resonance (^{1}H NMR) was employed to track liquid-phase products throughout the reaction. As shown in Fig. 3(b), the formate (FE_{HCOO^-}) remained above 90% within the potential range of −0.70 to −0.90 V vs. RHE, peaking at 98.7% at −0.70 V. Over the entire potential window, In Clu/C exhibited significantly higher FE_{HCOO^-} compared to In NC and In SACs/C (Figs. S12 and S13 in the ESM). These findings demonstrate the exceptional selectivity of In Clu/C for CO_2 reduction to formate. The partial current density for $HCOO^-$ (J_{HCOO^-}) across all catalysts within their respective potential ranges is clearly depicted in Fig. 3(c). Furthermore, the catalytic stability of In Clu/C was assessed at −0.70 V vs. RHE over a 50-hour period (Fig. 3(e)). At the conclusion of the stability test, there was no significant decrease in current density, and the FE_{HCOO^-} decreased slightly from 98.7% to 96.9%, indicating both high selectivity and good durability for In Clu/C. In addition, the key performance metrics (partial current density and Faraday efficiency) of In Clu/C and the other catalysts are summarized in Fig. 3(d), with detailed numerical comparisons provided in Tables S2 and S3 in the ESM. After the CO_2RR experiment, the In Clu/C catalyst was analyzed by EXAFS, and no significant structural changes were observed, as shown in Fig. S14 in the ESM.

To elucidate the changes in the atomic and electronic structure of In Clu/C during the CO_2RR, potential-dependent *in-situ* XAFS measurements were conducted [50, 51]. Real-time XAFS spectra were acquired using a self-constructed *in-situ* electrochemical cell for the CO_2RR. The In K-edge spectra were obtained in a 0.5 M $KHCO_3$ solution saturated with CO_2 at applied potentials of −0.2, −0.6, and −1.0 V vs. RHE. As shown in Fig. 4(a), the absorption edge in the In K-edge XANES spectra shifted to lower energy, accompanied by a decrease in the white line peak intensity. These observations are primarily attributed to the reduction in the oxidation state of the indium clusters during the charge transfer process between $In^{\delta+}$ and CO_2 molecules, as illustrated in Figs. 4(b) and 4(c). To further investigate the changes in the local atomic structure, we also analyzed the *in-situ* EXAFS spectra (Figs. 4(d) and 4(e)). The k^3-weighted FT-EXAFS spectra still exhibit a main peak and a shoulder peak, which are primarily attributed to the interaction between indium and carbon, as well as the In–In interaction. Notably, the In–O/C peak position in In Clu/C shifted slightly from 1.49 to 1.46 Å, indicating a reduction in the average In–O/C distance during the CO_2RR process. The atomic structure surrounding indium was extracted using a quantitative EXAFS analysis (Figs. S15–S17 and Table S4 in the ESM). Based on the fitting results, during the CO_2RR, the interaction between the In moieties and CO_2 molecules contributes to the enhanced CO_2RR

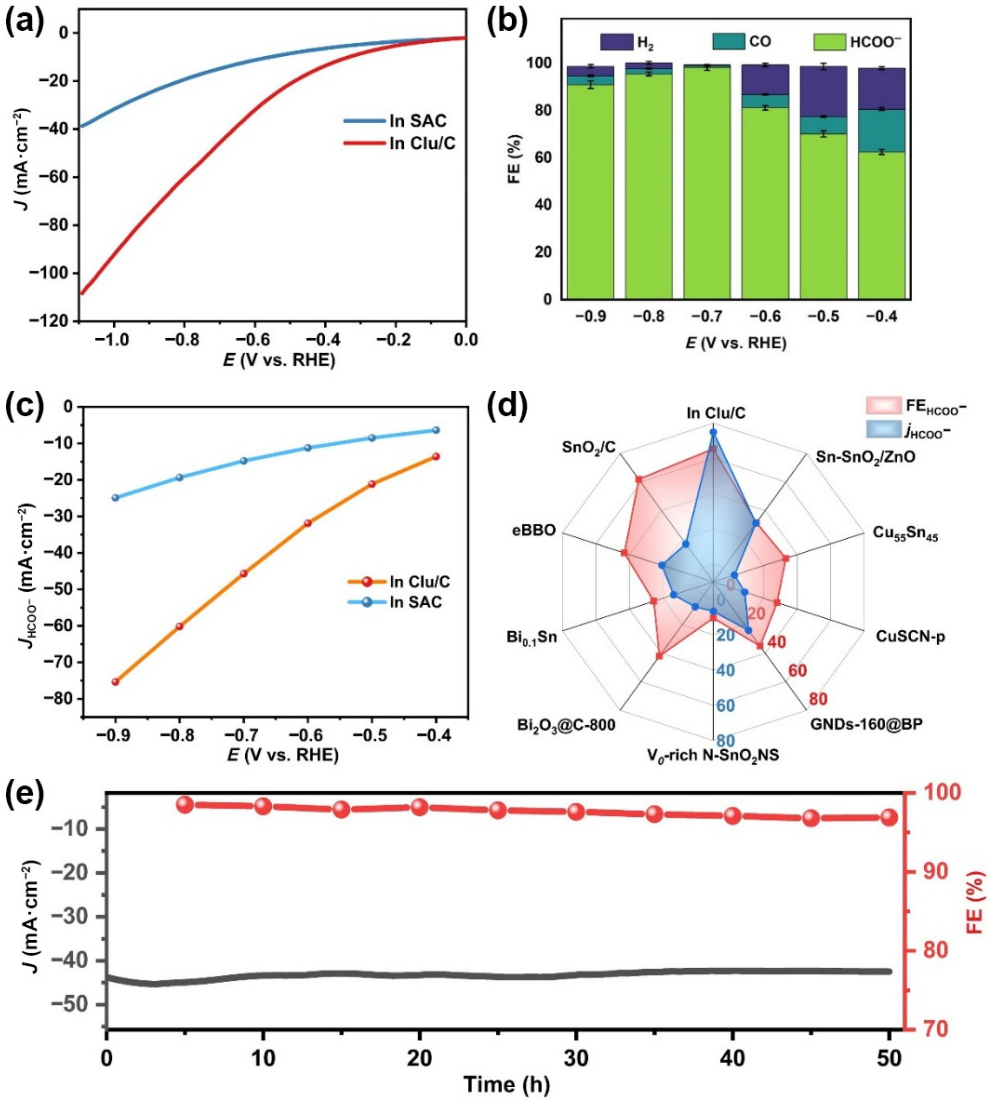

Figure 3 (a) LSV curves of In Clu/C and In SACs/C performed in CO_2-saturated 0.5 M $KHCO_3$. (b) Potential-dependent FEs for $HCOO^-$, CO, and H_2. (c) J_{HCOO^-} of In Clu/C and In SACs/C. (d) Formate FEs of In Clu/C compared with those of other catalysts for CO_2 to $HCOO^-$ reduction in Table S2 in the ESM. (e) Long-term stability of In Clu/C.

activity of In Clu/C, potentially altering its local configuration. Furthermore, *in-situ* attenuated total reflectance Fourier transform infrared spectroscopy (ATR-FTIR) was employed to detect the key intermediates in the CO_2 reduction reaction (Fig. S18 in the ESM). Initially, no distinct group signals were observed. In experimental tests carried out on the In Clu/C catalyst, a prominent peak corresponding to *OCHO at approximately 1300 cm^{-1} was detected. This peak showed an increasing intensity as the applied potentials were lowered. Moreover, the results demonstrated that In Clu/C did not adsorb significant amounts of CO* intermediates during the reaction, suggesting that CO was not the major product. The above results suggest that, during the CO_2RR process, the conversion of CO_2 to formate (*OCHO) on the In NC catalyst is more efficient compared to the conversion to *COOH.

In-situ XAFS and *In-situ* ATR-FTIR analysis suggests that the improved CO_2 reduction performance of In Clu/C may be attributed to changes in the electronic structure of $In^{\delta+}$ at the atomic interface. Drawing from these findings, we propose a possible mechanism for CO_2RR, as illustrated in Fig. 5. The different types of indium atoms in the indium cluster are labeled with distinct colors: blue atoms represent those that bond directly to the carbon substrate, while purple atoms indicate those within the metal cluster that bond to other metal atoms but not to the carbon substrate. In a typical scenario, CO_2 molecules adsorb onto the surface of indium clusters that are anchored on nitrogen-free carbon. The adsorbed CO_2 subsequently accepts electrons from the working electrode and combines with protons (H^+) from the electrolyte to form the HCOO* intermediate. Following this, the HCOO* intermediate acquires an additional electron, resulting in the formation of adsorbed $HCOO^-$(ads). Ultimately, the adsorbed $HCOO^-$(ads) desorbs from the catalyst surface and enters the electrolyte.

4 Conclusions

In conclusion, we have investigated a novel nitrogen-free carbon-supported indium cluster catalyst that demonstrates high efficiency for CO_2RR. The *in-situ* XAS analysis indicates that the exceptional CO_2RR performance is attributed to the distinctive $In^{\delta+}$ active sites. These results provide valuable guidance for the rational design of

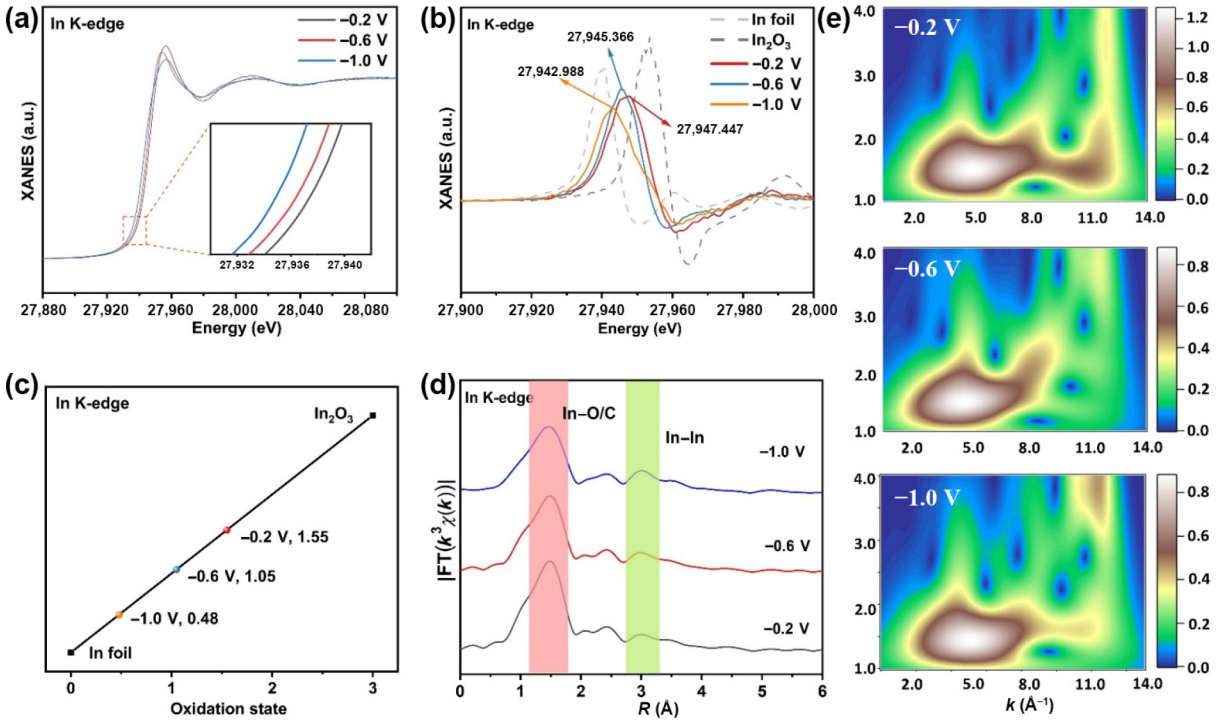

Figure 4 (a) In K-edge XANES spectra of In Clu/C at various potentials during CO_2RR. (b) The first-derivative XANES curves of In Clu/C at In K-edge. (c) The changing trend of the oxidation state at In K-edge for CO_2RR. (d) *In-situ* In K-edge k^3 FT-EXAFS at −0.2, −0.6, and −1.0 V vs. RHE. (e) WT-EXAFS plots of In Clu/C at −0.2, −0.6, and −1.0 V vs. RHE.

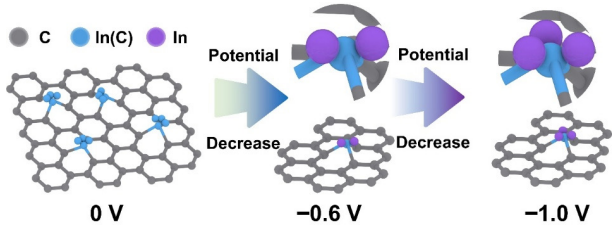

Figure 5 The scheme of catalytically active In Clu/C is proposed based on operando XAS analysis.

metal cluster catalysts tailored for environmental and energy conversion applications.

Electronic Supplementary Material: Supplementary material (XAFS measurements, XAFS data processing, TEM and XRD) is available in the online version of this article at https://doi.org/10.26599/NR.2025.94907370.

Data availability

All data needed to support the conclusions in the paper are presented in the manuscript and the Electronic Supplementary Material. Additional data related to this paper may be requested from the corresponding author upon request.

Acknowledgements

This work was supported by the National Natural Science Foundation of China (No. 22201262), Natural Science Foundation of Henan (No. 252300421175), the University Natural Science Research Project of Anhui Province (No. 2024AH040186), and the Application Project of Bengbu Univerisity (No. 2024YYX28QD). The authors thank the BL14W1 in the Shanghai Synchrotron Radiation Facility (SSRF) and BL10B and BL12B in the National Synchrotron Radiation Laboratory (NSRL) for help with characterization.

Declaration of competing interest

The authors declare that they have no known competing financial interests or personal relationships that could have appeared to influence the work reported in this paper.

Author contribution statement

H. S. S., F. Y., and Y. F. L. conceived the idea, designed the study and wrote the paper. X. L. and Y. T. L. performed most of the reactions, collected and analyzed the data, and wrote the paper. Y. G. and H. S. S. checked the paper, performed some of the experiments, and revised the paper.

Use of AI statement

None.

References

[1] Chu, S.; Majumdar. A. Opportunities and challenges for a sustainable energy future. *Nature* **2012**, *488*, 294–303.

[2] Chu, S.; Cui, Y.; Liu. N. The path towards sustainable energy. *Nat. Mater.* **2017**, *16*, 16–22.

[3] Stamenkovic, V. R.; Strmcnik, D.; Lopes, P. P.; Markovic. N. M. Energy and fuels from electrochemical interfaces. *Nat. Mater.* **2017**, *16*, 57–69.

[4] Zhan, Z. H.; Sun, Z. Y.; Wei, Z. H.; Li, Y. Q.; Chen, W. X.; Li, S. H.; Pang, S. P. Atomic interface regulation of rare-marth metal single

atom catalysts for energy conversion. *Nano Res.* **2024**, *17*, 3493–3515.
[5] Deng, Z. W.; Liu, Y.; Lin, J.; Chen, W. X. Rational design and energy catalytic application of high-loading single-atom catalysts. *Rare Met.* **2024**, *43*, 4844–4866.
[6] Shang, H. S.; Liu, D. Atomic design of carbon-based dual-metal site catalysts for energy applications. *Nano Res.* **2023**, *16*, 6477–6506.
[7] Gu, H. L.; Wu, J.; Zhang, L. M. Recent advances in the rational design of single-atom catalysts for electrochemical CO_2 reduction. *Nano Res.* **2022**, *15*, 9747–9763.
[8] Li, Q.; Wang, Y. C.; Zeng, J.; Zhao, X.; Chen, C.; Wu, Q. M.; Chen, L. M.; Chen, Z. Y.; Lei, Y. P. Bimetallic chalcogenides for electrocatalytic CO_2 reduction. *Rare Met.* **2021**, *40*, 3442–3453.
[9] Zhang, W.; Jia, B. H.; Liu, X.; Ma, T. Y. Surface and interface chemistry in metal-free electrocatalysts for electrochemical CO_2 reduction. *SmartMat* **2022**, *3*, 5–34.
[10] Wang, B. Q.; Chen, S. H.; Zhang, Z. D.; Wang, D. S. Low-dimensional material supported single-atom catalysts for electrochemical CO_2 reduction. *SmartMat* **2022**, *3*, 84–110.
[11] Zhou, X. L.; Liu, H.; Xia, B.; Ostrikov, K. Zheng, Y. ; Qiao, S. Z. Customizing the microenvironment of CO_2 electrocatalysis via three-phase interface engineering. *SmartMat* **2022**, *3*, 111–129.
[12] Pei, J. J.; Yang, L.; Lin, J.; Zhang, Z. D.; Sun, Z. Y.; Wang, D. S.; Chen, W. X. Integrating host design and tailored electronic effects of yolk–shell Zn-Mn diatomic sites for efficient CO_2 electroreduction. *Angew. Chem., Int. Ed.* **2024**, *63*, e202316123.
[13] Li, L. L.; Hasan, I. M. U.; Farwa; He, R. N.; Peng, L. W.; Xu, N. N.; Niazi, N. K.; Zhang, J. N.; Qiao, J. L. Copper as a single metal atom based photo-, electro-, and photoelectrochemical catalyst decorated on carbon nitride surface for efficient CO_2 reduction: A review. *Nano Res. Energy* **2022**, *1*, 9120015.
[14] Ahmad, T.; Liu, S.; Sajid, M.; Li, K.; Ali, M.; Liu, L.; Chen, W. Electrochemical CO_2 reduction to C_{2+} products using Cu-based electrocatalysts: A review. *Nano Res. Energy* **2022**, *1*, 9120021.
[15] Sun, Z. Y.; Li, C.; Wei, Z. H.; Zhang, F.; Deng, Z. W.; Zhou, K. J.; Wang, Y.; Guo, J. H.; Yang, J. Y.; Xiang, Z. Q. et al. Sulfur-bridged asymmetric CuNi bimetallic atom sites for CO_2 reduction with high efficiency. *Adv. Mater.* **2024**, *36*, 2404665.
[16] Sun, Z. Y.; Luo, X.; Shang, H. S.; Wang, Z. D.; Zhang, L.; Chen, W. X. Atomic printing strategy achieves precise anchoring of dual-copper atoms on C_2N structure for efficient CO_2 reduction to ethylene. *Angew. Chem., Int. Ed.* **2024**, *63*, e202405778.
[17] Yang, J. R.; Li, W. H.; Wang, D. S.; Li. Y. D. Electronic metal-support interaction of single-atom catalysts and applications in electrocatalysis. *Adv. Mater.* **2020**, *32*, 2003300.
[18] Li, W. H.; Yang, J. R.; Wang. D. S. Long-range interactions in diatomic catalysts boosting electrocatalysis. *Angew. Chem.* **2022**, *134*, e202213318.
[19] Wang, S. W.; Gao, Q.; Xu, C.; Jiang, S.; Zhang, M. Y.; Yin, X. J.; Peng, H. Q.; Liu, B.; Song, Y. F. Molecular surface functionalization of In_2O_3 to tune interfacial microenvironment for enhanced catalytic performance of CO_2 electroreduction. *Nano Res.* **2024**, *17*, 1242–1250.
[20] Zhang, W. H.; Ding, S. J.; Zhang, Q. S.; Yi, H.; Liu, Z. X.; Shi, M. L.; Guan, R. D.; Yue, L. Rare earth element-doped porous In_2O_3 nanosheets for enhanced gas-sensing performance. *Rare Met.* **2021**, *40*, 1662–1668.
[21] Shang, H. S.; Wang, T.; Pei, J. J.; Jiang, Z. L.; Zhou, D. N.; Wang, Y.; Li, H. J.; Dong, J. C.; Zhuang, Z. B.; Chen, W. X. et al. Design of a single-atom indium$^{\delta+}$-N_4 interface for efficient electroreduction of CO_2 to formate. *Angew. Chem., Int. Ed.* **2020**, *59*, 22465–22469.
[22] Jiang, Z. L.; Wang, T.; Pei, J. P.; Shang, H. S.; Zhou, D. N.; Li, H. J.; Dong, J. C.; Wang, Y.; Cao, R.; Zhuang, Z. B. et al. Discovery of main group single Sb–N_4 active sites for CO_2 electroreduction to formate with high efficiency. *Energy Environ. Sci.* **2020**, *13*, 2856–2863.
[23] Zhang, L.; Zhao, Z. J.; Gong, J. L. Nanostructured materials for heterogeneous electrocatalytic CO_2 reduction and their related reaction mechanisms. *Angew. Chem., Int. Ed.* **2017**, *56*, 11326–11353.
[24] Li, X. Y.; Rong, H. P.; Zhang, J. T.; Wang, D. S.; Li. Y. D. Modulating the local coordination environment of single-atom catalysts for enhanced catalytic performance. *Nano Res.* **2020**, *13*, 1842–1855.
[25] Ji, S. F.; Chen, Y. J.; Wang, X. L.; Zhang, Z. D.; Wang, D. S.; Li. Y. D. Chemical synthesis of single atomic site catalysts. *Chem. Rev.* **2020**, *120*, 11900–11955.
[26] Li, L.; Zhang, Z. C. Sn–Bi bimetallic interface induced by nano-crumples for CO_2 electroreduction to formate. *Rare Met.* **2022**, *41*, 3943–3945.
[27] Yan, J. X.; Ye, F. H.; Dai, Q. B.; Ma, X. Y.; Fang, Z. H.; Dai, L. M.; Hu, C. G. Recent progress in carbon-based electrochemical catalysts: From structure design to potential applications. *Nano Res. Energy* **2023**, *2*, e9120047.
[28] Liu, J. B.; Gong, H. S.; Ye, G. L.; Fei, H. L. Graphene oxide-derived single-atom catalysts for electrochemical energy conversion. *Rare Met.* **2022**, *41*, 1703–1726.
[29] Liu, K. Y.; Chen, P. W.; Sun, Z. Y.; Chen, W. X.; Zhou, Q.; Gao, X. The atomic interface effect of single atom catalysts for electrochemical hydrogen peroxide production. *Nano Res.* **2023**, *16*, 10724–10741.
[30] Shang, H. S.; Zhou, X. Y.; Dong, J. C.; Li, A.; Zhao, X.; Liu, Q. H.; Lin, Y.; Pei, J. J.; Li, Z.; Jiang, Z. L. et al. Engineering unsymmetrically coordinated Cu-S_1N_3 single atom sites with enhanced oxygen reduction activity. *Nat. Commun.* **2020**, *11*, 3049.
[31] Geng, H. L.; Wei, Z. H.; Li, Y. Q.; Deng, Z. W.; Li, L.; Wang, Y.; Zhai, H. Z.; Li, S. H.; Chen, W. X. Controlling the electron spin states of single-atom catalysts for enhanced electrocatalytic performances. *JES* **2024**, *1*, 3630.
[32] Iqbal, M. S.; Yao, Z. B.; Ruan, Y. K.; Iftikhar, R.; Hao, L. D.; Robertson, A. W.; Imran, S. M.; Sun, Z. Y. Single-atom catalysts for electrochemical N_2 reduction to NH_3. *Rare Met.* **2023**, *42*, 1075–1097.
[33] Liu, D. Y.; Zeng, Q.; Hu, C. Q.; Chen, D.; Liu, H.; Han, Y. S.; Xu, L.; Zhang, Q. B.; Yang, J. Light doping of tungsten into copper-platinum nanoalloys for boosting their electrocatalytic performance in methanol oxidation. *Nano Res. Energy* **2022**, *1*, 9120017.
[34] Inagaki, M.; Toyoda, M.; Soneda, Y.; Morishita, T. Nitrogen-doped carbon materials. *Carbon* **2018**, *132*, 104–140.
[35] Mamtani, K.; Jain, D.; Zemlyanov, D.; Celik, G.; Luthman, J.; Renkes, G.; Co, A. C.; Ozkan, U. S. Probing the oxygen reduction reaction active sites over nitrogen-doped carbon nanostructures (CN_x) in acidic media using phosphate anion. *ACS Catal.* **2016**, *6*, 7249–7259.
[36] Wang, S. C.; Zhang, M. Y.; Mu, X. Q.; Liu, S. L.; Wang, D. S.; Dai, Z. H. Atomically dispersed multi-site catalysts: Bifunctional oxygen electrocatalysts boost flexible zinc-air battery performance. *Energy Environ. Sci.* **2024**, *17*, 4847–4870.
[37] Mu, X. Q.; Zhang, X. Y.; Chen, Z. Y.; Gao, Y.; Yu, M.; Chen, D.; Pan, H. Z.; Liu, S. L.; Wang, D. S.; Mu, S. C. Constructing symmetry-mismatched $Ru_xFe_{3-x}O_4$ heterointerface-supported Ru clusters for efficient hydrogen evolution and oxidation reactions. *Nano Lett.* **2024**, *24*, 1015–1023.
[38] Ma, F. Y.; Zhang, P. F.; Zheng, X. B.; Chen, L.; Li, Y. R.; Zhuang, Z. C.; Fan, Y. M.; Jiang, P.; Zhao, H.; Zhang, J. W. et al. Steering the site distance of atomic Cu–Cu pairs by first-shell halogen coordination boosts CO_2-to-C_2 selectivity. *Angew. Chem., Int. Ed.* **2024**, *63*, e202412785.

[39] Mu, X. Q.; Liu, S. L.; Zhang, M. Y.; Zhuang, Z. C.; Chen, D.; Liao, Y. R.; Zhao, H. Y.; Mu, S. C.; Wang, D. S.; Dai, Z. H. Symmetry-broken Ru nanoparticles with parasitic Ru–Co dual-single atoms overcome the Volmer step of alkaline hydrogen oxidation. *Angew. Chem., Int. Ed.* **2024**, *63*, e202319618.

[40] Zhang, Y.; Mu, X. Q.; Liu, Z. Y.; Zhao, H. Y.; Zhuang, Z. C.; Zhang, Y. F.; Mu, S. C.; Liu, S. L.; Wang, D. S.; Dai, Z. H. Twin-distortion modulated ultra-low coordination PtRuNi-O_x catalyst for enhanced hydrogen production from chemical wastewater. *Nat. Commun.* **2024**, *15*, 10149.

[41] Chen, S. H.; Zheng, X. B.; Zhu, P.; Li, Y. P.; Zhuang, Z. C.; Wu, H. J.; Zhu, J. X.; Xiao, C. H.; Chen, M. Z.; Wang, P. S. et al. Copper atom pairs stabilize *OCCO dipole toward highly selective CO_2 electroreduction to C_2H_4. *Angew. Chem., Int. Ed.* **2024**, *63*, e202411591.

[42] Gu, X. Y.; Yu, M.; Chen, S. Q.; Mu, X. Q.; Xu, Z. H.; Shao, W. Q.; Zhu, J. J.; Chen, C. Y.; Liu, S. L.; Mu, S. C. Coordination environment of Ru clusters with *in-situ* generated metastable symmetry-breaking centers for seawater electrolysis. *Nano Energy* **2022**, *102*, 107656.

[43] Chen, J. G. NEXAFS investigations of transition metal oxides, nitrides, carbides, sulfides and other interstitial compounds. *Surf. Sci. Rep.* **1997**, *30*, 1–152.

[44] Chen, P. Z.; Zhang, N.; Wang, S. B.; Zhou, T. P.; Tong, Y.; Ao, C. C.; Yan, W. S.; Zhang, L. D.; Chu, W. S.; Wu, C. Z. et al. Interfacial engineering of cobalt sulfide/graphene hybrids for highly efficient ammonia electrosynthesis. *Proc. Natl. Acad. Sci. USA* **2019**, *116*, 6635–6640.

[45] Li, Y.; Wang, X.; Wang, Y.; Shi, Z. P.; Yang, Y. Q.; Zhao, T.; Jiang, Z.; Liu, C. P.; Xing, W.; Ge, J. J. The decisive role of adsorbed OH* in low-potential CO electro-oxidation on single-atom catalytic sites. *Carbon Energy* **2023**, *5*, e310.

[46] Liu, M. H.; Liu, S. J.; Xu, Q.; Miao, Q. Y.; Yang, S.; Hanson, S.; Chen, G. Z.; He, J.; Jiang, Z.; Zeng, G. F. Dual atomic catalysts from COF-derived carbon for CO_2RR by suppressing HER through synergistic effects. *Carbon Energy* **2023**, *5*, e300.

[47] Gates, B. C. Supported metal clusters: Synthesis, structure, and catalysis. *Chem. Rev.* **1995**, *95*, 511–522.

[48] Li, X. N.; Yang, X. F.; Zhang, J. M.; Huang, Y. Q.; Liu. B. *In situ*/operando techniques for characterization of single-atom catalysts. *ACS Catal.* **2019**, *9*, 2521–2531.

[49] Rehr, J. J.; Albers, R. C. Theoretical approaches to X-ray absorption fine structure. *Rev. Mod. Phys.* **2000**, *72*, 621–654.

[50] Gandionco, K. A.; Kim, J.; Bekaert, L.; Hubin, A.; Lim, J. Single-atom catalysts for the electrochemical reduction of carbon dioxide into hydrocarbons and oxygenates. *Carbon Energy* **2024**, *6*, e410.

[51] Fang, L. Z.; Seifert, S.; Winans, R. E.; Li, T. Operando XAS/SAXS: Guiding design of single-atom and subnanocluster catalysts. *Small Methods* **2021**, *5*, 2001194.